An experimental 2DVAR retrieval using AMSR2

David Ian Duncan[1], Patrick Eriksson[1], and Simon Pfreundschuh[1]

[1]Department of Earth, Space, and Environment, Chalmers University of Technology, SE 412 96 Gothenburg, Sweden

Correspondence: David Ian Duncan (david.duncan@chalmers.se)

Abstract. A two-dimensional variational retrieval (2DVAR) is presented for a passive microwave imager. The overlapping antenna patterns of all frequencies from the Advanced Microwave Scanning Radiometer-2 (AMSR2) are explicitly simulated to attempt retrieval of near surface wind speed and surface skin temperature at finer spatial scales than individual antenna beams. This is achieved, with the effective spatial resolution of retrieved parameters shown by analysis of 2DVAR averaging kernels.

5 Sea surface temperature retrievals achieve about 30 km resolution, with wind speed retrievals at about 10 km resolution. It is argued that multi-dimensional optimal estimation permits greater use of total information content from microwave sensors than other methods, with no compromises on target resolution needed; instead, various targets are retrieved at the highest possible spatial resolution, driven by the channels' sensitivities. All AMSR2 channels can be simulated within near their published noise characteristics for observed clear-sky scenes, though calibration and emissivity model errors are key challenges. This

10 experimental retrieval shows the feasibility of 2DVAR for cloud-free retrievals, and opens the possibility of standalone 3DVAR retrievals of water vapour and hydrometeor fields from microwave imagers in the future. The results have implications for future satellite missions and sensor design, as spatial oversampling can somewhat mitigate the need for larger antennas in the push for higher spatial resolution.

1 Introduction

15 Observations from satellites at microwave frequencies for which the Earth's atmosphere is relatively transparent, so-called imaging channels, provide valuable information to constrain estimates of skin temperature, wind speed, sea ice concentrations, soil moisture, and more. With global coverage, relative insensitivity to clouds, and a decades-long data record, microwave radiometers provide complementary information alongside infrared and scatterometer retrievals that may possess higher accuracy or higher resolution but have limitations in coverage (Atlas et al., 2011; Reynolds et al., 2007). Additionally, due to

20 microwave imager channels' multiple sensitivities, simultaneous retrieval of multiple parameters with one observation vector ensures some geophysical consistency in the retrieved state vector (e.g. Phalippou, 1996; Bettenhausen et al., 2006; Munchak et al., 2016; Duncan et al., 2018). In operational contexts, assimilation of microwave imager radiances sensitive to skin temperature, humidity, and winds can add to forecast skill in various ways (Geer et al., 2017; Singh et al., 2008; Kazumori et al., 2016).

25 Lower frequency microwaves have the best sensitivity to the Earth's surface, in this context constituting frequencies of about 10 GHz and below, with wavelengths of about 3 cm and more, known also as the X- and C-bands. These bands are valuable for

Earth observation because the atmosphere attenuates these signals very little, with thermal emission from the Earth's surface impeded only slightly by water vapor and precipitation. Apart from radio frequency interference (RFI) being common at these frequencies due to the utility of non-attenuating bands for telecommunications (Draper, 2018; Zabolotskikh et al., 2015), the main drawback of these frequencies for Earth observation is their spatial resolution, which is driven by laws of diffraction. The spatial extent of one satellite pixel is determined by the observation frequency, orbit altitude, and antenna size. With the satellite's altitude fixed, the spatial resolution is linearly proportional to the ratio of wavelength to reflector diameter.

The largest passive microwave reflectors yet flown for Earth observation include the JAXA Global Change Observation Mission Water 1 (GCOM-W1; Imaoka et al. (2010)) with the Advanced Microwave Scanning Radiometer 2 (AMSR2), which features a $2.0\,\mathrm{m}$ solid reflector, and NASA's Soil Moisture Active Passive (SMAP) satellite with a $6\,\mathrm{m}$ deployable reflector (Entekhabi et al., 2010). Both of these have real aperture antennas; because large solid reflectors cause concerns over their mass, drag, and transport into orbit, other antenna types are being explored (Kilic et al., 2018). But even with larger antennas, the trade off between sensor size and resolution on the ground remains.

However, a hidden advantage of observation at these bands lies in the spatial oversampling that is a byproduct of the large field of view (FOV) of each channel. Essentially, because the footprints are so large, they overlap significantly both along individual scans and between scans. This characteristic can be exploited by averaging or smoothing as a way to beat down the sensor noise, such as by averaging each channel's radiometric signal on an equal area grid before running a retrieval (Meier et al., 2017). But this further smears the low resolution of the large FOVs and discards any finer-scale information that may exist in the measurements.

Spatial oversampling of satellite radiometry should permit retrieved quantities to achieve greater robustness and a higher effective spatial resolution. As with photographic images, satellite imagery can benefit from techniques that allow finer spatial scales to be realised and crisper, more detailed images to emerge. However, as wavelength increases, physical constraints limit the design of radiometers, necessitating ever larger antennas to achieve finer spatial resolution (e.g. Kilic et al., 2018; Entekhabi et al., 2010). This is a design constraint when observing geophysical properties best sensed via low frequency microwaves. This has been an issue for past satellite sensors and will remain a challenge for maximal use of future sensors such as the MicroWave Imager (MWI) and Ice Cloud Imager (ICI) on MetOp-SG, which will also be heavily over-sampled.

To put the spatial oversampling of microwave imagers into context, it is worth examining the lowest frequency channels of AMSR2. The $6.925\,\mathrm{GHz}$ channels on AMSR2 observe the Earth's surface with a half-power beam width (HPBW) of $35\,\mathrm{km}$ by $62\,\mathrm{km}$ in the across- and along-track directions, respectively, defining their instantaneous FOV (IFOV). The AMSR2 produces 243 pixels across one scan, spanning about $1450\,\mathrm{km}$, and approximately 4000 scans per orbit. The average scans are $10\,\mathrm{km}$ apart along-track, with the average pixel centres just $9\,\mathrm{km}$ apart across-track at swath centre and closer at the swath's edge. To treat adjacent pixels at low frequency channels as having wholly independent information is demonstrably problematic, as a large percentage of the information is redundant. The relative overlap of AMSR2 beams on the Earth's surface and the large variations of FOV size with frequency can be seen in Fig. 1.

For some retrieval targets such as precipitation, there is little spatial coherence to an image, or spatial correlations are highly variable. But for a retrieval target like sea surface temperature (SST) or ocean wind speeds, a priori knowledge of its spatial
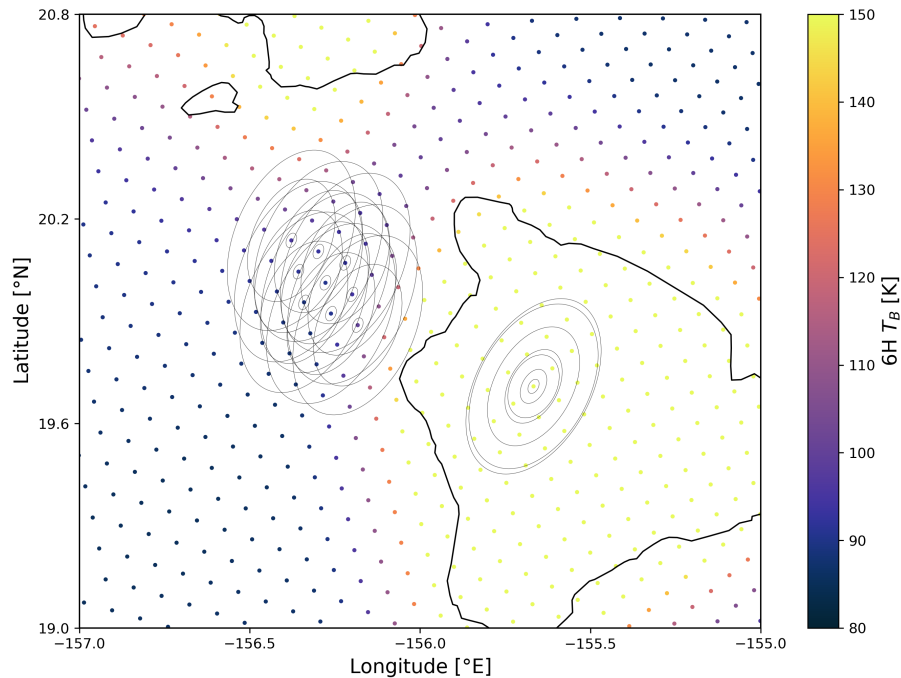
Figure 1. An example of FOV sizes and measured T_B at the 6H channel near the Island of Hawai'i, from an ascending AMSR2 orbit on September 21, 2016. The T_Bs at 6H are shown in coloured dots, with the HPBW given at all AMSR2 frequencies for one pixel viewing the island itself. The HPBW is outlined for three channels only (6, 10, 89GHz) for three consecutive pixels and scans just west of the island, to view the spatial overlap without too much clutter.

structures can be brought to bear on the inversion problem as a further constraint. Sub-mesoscale fluctuations in SST fields can exist (Castro et al., 2017), but most oceanic near-surface wind speed variability is synoptically forced and thus spatial decorrelation lengths are significant. Wind retrievals can also benefit from accounting for spatial correlations for ambiguity removal (Vogelzang and Stoffelen, 2018; Lin et al., 2016). Ideally, spatial covariances of each field can be included in a

5 retrieval scheme, and even cross-correlations between variables. The common practice of treating neighboring satellite pixels as wholly independent retrieval targets thus represents a suboptimal use of the total information content of the observation vector, especially considering the substantially overlapping FOVs of adjacent pixels (Fig. 1).

The dependence of FOV size on frequency has led to convolution and de-convolution approaches (e.g. Backus and Gilbert, 1967; Petty and Bennartz, 2017) to construct a common spatial resolution for performing retrievals. This can be crucial for

10 1DVAR retrievals with scene inhomogeneities (Rapp et al., 2009). However, the optimal observation resolution depends upon the retrieval target, may vary over the scene, and is not known a priori. The choice of a common spatial resolution is a compromise and adds noise to some of the observed quantities. In contrast, a 2DVAR approach permits usage of all native resolution observations with no compromises required. If the various beam sizes, angles, positions, and antenna patterns are accounted for in the forward model, and spatial homogeneity within the beam is not required because the forward model

contains horizontal dimensions, then it is possible to rely on fewer assumptions. If the beams are adequately simulated and the retrieval grid is finer than the beam widths, 2DVAR (or 3DVAR) thus offers an opportunity to use the native resolution observations without resampling or compromise, a maximal usage of the available information content.

One hallmark of data assimilation is the inclusion of many variables and their covariances as part of a multidimensional minimisation procedure to determine the geophysical state. A purely variational assimilation in the three spatial dimensions is known as 3DVAR, or 4DVAR if a time component is included as well. Standalone remote sensing retrievals also endeavour to solve for the geophysical state but typically have a much more limited scope, both spatially and in terms of the state vector. Satellite retrievals may use any method to invert the measurement vector, but retrievals are usually treated independently in space and time, with no knowledge of adjacent pixels. In other words, each pixel of the image is treated separately. So while 1DVAR retrieval methods are common for satellite retrievals (e.g. Boukabara et al., 2011; Elsaesser and Kummerow, 2008; Duncan and Kummerow, 2016), the horizontal spatial dimensions are usually disregarded for downward-viewing sensors. As weather models progress to spatial resolutions finer than some satellite FOVs, the need for better use of satellite sensors' inherent spatial information will only increase. Furthermore, as full utilisation of sensors' information is a goal of data assimilation, any approach that can make better use of the spatial information contained in satellite observations has potential benefits for future data assimilation efforts.

In the following section, the theory behind 2DVAR and its application in this study are given. The sensor and forward model are then described in detail, as are the covariances and a priori information used in the 2DVAR inversion. Synthetic retrieval results are presented in Section 4 and real observational results using AMSR2 data are presented in Section 5. Discussion and conclusions close the paper.

2 2DVAR

2.1 Theory

The optimal estimation methodology is a Bayesian inversion that balances prior knowledge and its known errors with the information gained by measurements with their own errors (Rodgers, 2000). Via variational iteration, optimal estimation attempts to minimise the following cost function that balances the a priori state vector (x_a) and the measurement vector (y) to invert the measurement with a forward model operator ($f(x)$) and determine the state vector (x) of maximum posterior likelihood:

$$\Phi = (y - f(x))^T \mathbf{S_y}^{-1}(y - f(x)) + (x - x_a)^T \mathbf{S_a}^{-1}(x - x_a) \qquad (1)$$

The observation operator covariance matrix ($\mathbf{S_y}$) and a priori covariance matrix ($\mathbf{S_a}$) determine the trust placed in the measurement vector and a priori knowledge. In the context of passive microwave satellite retrievals, these are typically 1-dimensional variational retrievals, or 1DVAR (Boukabara et al., 2011; Duncan and Kummerow, 2016; Pearson et al., 2018), as the state vector has a vertical dimension but no other spatial dimensions. This cost function (Eq. 1) is applicable for inverse problems containing zero to n dimensions, and can thus be adapted from a 1DVAR retrieval to handling retrieval targets of multiple variables in n-dimensional space. Gaussian-distributed errors are assumed in this methodology.

An important byproduct of optimal estimation is its estimation of the posterior probability density function of the retrieved state, providing users with a representation of the errors and covariances of retrieved parameters. This is described by $\mathbf{S_x}$,

$$\mathbf{S_x} = (\mathbf{K}^T \mathbf{S_y}^{-1} \mathbf{K} + \mathbf{S_a}^{-1})^{-1} \tag{2}$$

where $\mathbf{K}$ is the Jacobian defined by the first derivative of $f(x)$ to changes in the state vector.

5   The averaging kernel matrix $\mathbf{A}$ is defined in relation to the Jacobian $\mathbf{K}$ and the covariance matrices $\mathbf{S_y}$ and $\mathbf{S_a}$, with its interpretation being the sensitivity of the retrieval to the true state, $\hat{x}$.

$$\mathbf{A} = (\mathbf{K}^T \mathbf{S_y}^{-1} \mathbf{K} + \mathbf{S_a}^{-1})^{-1} \mathbf{K}^T \mathbf{S_y}^{-1} \mathbf{K} = \frac{\delta \hat{x}}{\delta x} \tag{3}$$

The averaging kernel also helps to define the smoothing error of the retrieval, $\mathbf{S_s}$, in which $\mathbf{I}$ is the identity matrix.

$$\mathbf{S_s} = (\mathbf{A} - \mathbf{I}) * \mathbf{S_a} * (\mathbf{A} - \mathbf{I}) \tag{4}$$

10   Rows of $\mathbf{A}$ will sum to 1.0 (along the respective block of the sparse matrix) for retrieved variables for which the retrieval has full sensitivity with regard to the true state (Rodgers, 2000). This is sometimes referred to as the "measurement response", and will differ for each retrieved parameter at all retrieval grid points. Later in the study, rows of $\mathbf{A}$ are translated into the 2D space of the retrieval grid and examined as the measurement response for each retrieved parameter, indicating the spatial resolution achieved by the inversion for these retrieval targets. The trace of $\mathbf{A}$ defines the degrees of freedom for signal (DFS), or the

15   total number of retrieved variables fully constrained by the retrieval. It is worth noting that the obtained $\mathbf{A}$ and $\mathbf{S_x}$ are both dependent upon the assumed covariances of the a priori state, $\mathbf{S_a}$, and observation operator, $\mathbf{S_y}$, and thus their interpretation relies on realistic user inputs for the elements in these matrices.

2.2   Retrieval setup

Following the terms presented in Eq. 1, here are detailed the covariances and a priori information used within the 2DVAR

20   inversion. The a priori state (x_a) for SST and $10\,\mathrm{m}$ wind speed (hereafter WSP) in the synthetic case are defined simply as the field mean for all points in the retrieval grid; in the real cases, x_a comes from reanalysis data interpolated to the retrieval grid. For all cases, the first guess values are the means of the x_a fields.

A priori covariances ($\mathbf{S_a}$) are defined by a non-diagonal matrix, as non-zero spatial correlations are assumed for the parameters. For the cases presented, no cross correlation is prescribed between SST and WSP. The diagonal terms in $\mathbf{S_a}$ are fixed

25   at 1.5 for both SST and WSP, indicating an assumed standard deviation of $1.5\,\mathrm{K}$ and $1.5\,\mathrm{m\,s}^{-1}$. Off-diagonal terms in $\mathbf{S_a}$ are calculated via a decorrelation distance (ℓ_d) and the proximity of each retrieval grid point in space, with the distance between grid points i and j given by $d_{i,j}$.

$$\mathbf{S_a}(i,j) = \sigma_a^2 \exp(-\ell_d / d_{i,j}) \tag{5}$$

In all retrieval cases described, ℓ_d is prescribed as $1.0°$ in latitude and longitude. The retrieval grid spacing is set independently,

30   and can be set separately for different retrieved parameters. For simplicity, the retrieval grid for both SST and WSP is set at

Table 1. Sensor characteristics of AMSR2 aboard JAXA's GCOM-W1 satellite. Vertically and horizontally polarised channels are notated by 'V' and 'H,' respectively. Note that additional 89GHz channels exist on AMSR2 but are not included as they were not used here.

Centre Frequency [GHz]	6.925	7.3	10.65	18.7	23.8	36.5	89.0
Polarisations	V, H	V, H	V, H	V, H	V, H	V, H	V, H
Bandwidth [MHz]	350	350	100	200	400	1000	3000
NEDT [K]	0.34	0.43	0.70	0.70	0.60	0.70	1.20
Angular beam width [°]	1.80	1.80	1.20	0.65	0.75	0.35	0.15
IFOV width [km]	35	34	24	14	15	7	3
IFOV height [km]	62	58	42	22	26	12	5

$0.05°$ in latitude and longitude. Note that this is finer than the spacing of most AMSR2 pixels on the Earth's surface and indeed most global weather models, but in line with grid resolutions applied for scatterometers (Vogelzang and Stoffelen, 2017). If a near-zero decorrelation length were used, a coarser retrieval grid would be needed.

Observation error covariances ($\mathbf{S_y}$) are quite simple for this retrieval, with no off-diagonal terms considered. The matrix is
5   diagonal, consisting of the published sensor noise characteristics for every channel (Table 1), increased by a factor of 2.0 for the real world retrievals to somewhat compensate for the existence of forward model and parameter errors. The diagonal $\mathbf{S_y}$ makes the inversion simpler and faster. For example, since an inversion of 14 channels for an observation space of 20 scans with 25 pixels each constitutes an observation vector (y) of 7000 elements, this is not trivial. Whereas some studies include covariances between co-registered observations due to correlated forward model errors (Weston et al., 2014; Bormann et al.,
10   2016; Duncan et al., 2018), it is unclear whether sensor noise or other errors have any spatial correlations. The nature of sensor noise and its assumed characteristics pixel to pixel, i.e. Gaussian and random, will be a topic raised again in Section 6.

3   Data and Methods

3.1   GCOM-W1 AMSR2

The AMSR2 sensor flies on JAXA's GCOM-W1 satellite, which was launched in May 2012. Due to its numerous low frequency
15   microwave imaging channels sensitive to the surface, it is the sensor of interest for this study. The channels available on AMSR2 and their characteristics are given in Table 1. GCOM-W1 flies in a sun-synchronous low Earth orbit of inclination $98.2°$ with ascending node crossing the equator at 13:30 local time, part of the A-Train constellation, at a nominal altitude of $700\,km$. AMSR2 is a conically scanning radiometer, maintaining a near-constant Earth incidence angle of $55°$ via a sensor angle of $47.5°$ off nadir.
20   Two main factors for retrieval performance with AMSR2 are its channels' noise characteristics, given as noise equivalent differential temperature (NEDT), and its instantaneous field of view (IFOV), given in kilometers and indicative of its HPBW as defined by an ellipse on the Earth's surface. These two characteristics change for each channel, affecting the precision

and spatial extent of each individual observation's radiometric information. The sensor noise and FOV ultimately limit the accuracy of retrieval quantities, which for a variational retrieval can be investigated in terms of its posterior uncertainty and spatial smoothing error (Eq. 4).

All observational data used from AMSR2 come from JAXA's L1R product (Maeda et al., 2016). This data product contains
5   resampled brightness temperatures (T_Bs) at various channels, but only the native resolution T_Bs are used in this study. In addition, the spacecraft's location and the latitude/longitude pair for each AMSR2 bore sight location on Earth are used to explicitly define the sensor line of sight through Earth's atmosphere.

Sensor calibration and its relative agreement with the forward model are of paramount importance for the success of a retrieval. In the case of SST retrieval, for example, the ocean surface emissivity is on order 0.55 and 0.25 for the 6V and 6H
10   channels at 55° Earth incidence angle, respectively, and thus a systematic calibration bias of only $0.5\,\mathrm{K}$ could translate to a $1.0\,\mathrm{K}$ SST bias. Due to previous success using the intercalibration tables from the Global Precipitation Measurement (GPM) mission (Berg et al., 2016) with a similar forward model (Duncan and Kummerow, 2016; Duncan et al., 2017), the AMSR2 channels used in the GPM constellation ($10\,\mathrm{GHz}$ and up) in this study use the GPM calibration (Berg, 2016). To make the 6V/6H/7V/7H channels consistent with this calibration, ad hoc adjustments were calculated and applied to return zero net
15   bias at these channels over several orbits forced with reanalysis data and using the retrieval's forward model. The 6V and 7V calibration offsets applied are -0.46K and -0.63K, versus -2.59K and -3.12K for 6H and 7H. However, the calibration used here is far from definitive, due to the non-linear calibration adjustments inherent in the L1R data (which are largest for the lowest frequency channels), the ad hoc nature of the adjustments performed, and the limited scope of this analysis. A different forward model would require different calibration adjustments.

3.2   Forward model

As the forward model of the 2DVAR retrieval presented here is novel and key to its understanding, it is explained in detail. The forward model and the 2DVAR solver itself both defined within the Atmospheric Radiative Transfer Simulator (ARTS) V2.3 (Eriksson et al., 2011; Buehler et al., 2018); ARTS permits 3-dimensional polarised radiative transfer, which is necessary for the forward model. All code to call the ARTS model, set up the inversion, and analyze the retrieval output were written
25   in Jupyter Notebooks using the Python package Typhon v0.7.0 (The Typhon Authors), and are publicly available (Duncan, 2019). In this section and throughout the paper, "scan" refers to each set of observations swept out by the radiometer in one rotation, throughout which spacecraft position is assumed constant; "pixel" refers to points within a scan, which is a vector of T_Bs observed simultaneously and centered at one point on Earth's surface but with different antenna patterns. Thus pixels are points in the across-track direction, with numerous pixels per scan, while successive scans are in the along-track direction
30   relative to the spacecraft's motion vector. For reference, the AMSR2 L1R data contain 243 (low frequency) pixels per scan and thus the sample cases presented here represent a fraction of the total swath width.

A geophysical space is defined on a regular latitude and longitude grid, with a pressure grid defining that atmosphere above. For the synthetic cases in this study, a typical tropical atmospheric profile is assumed for temperature and water vapour; for the real observations, atmospheric profiles come from the European Centre for Medium-range Weather Forecasting (ECMWF)

Reanalysis 5 (ERA5). The atmospheric grid matches the pressure levels from ERA5, from sea level up to $100\,\mathrm{hPa}$. Within the geophysical space, an independent retrieval grid is defined with its own spatial resolution and edges. In the examples given, all observations lie within the confines of the retrieval grid, and the retrieval grid is entirely within the larger geophysical grid. The term "observation space" will refer to the area of the retrieval grid well populated by observations.

5   Each AMSR2 scan is treated as a measurement block in ARTS, connecting each individual pixel. The measurement block is then described in angular space as deviations from the center bore sight of the scan, in zenith (θ, along-track) and azimuth (ϕ, across-track). Sampling of this measurement space is then accomplished by performing numerous "pencil beam" radiative transfer calculations on a defined angular grid in the 3D space. This angular grid's resolution is chosen based on the density of sampling desired of the antenna patterns and geophysical space. The pencil beam grid has a prescribed number of points

10   between each bore sight, with this angular resolution also used in the zenith direction to keep consistent sampling between scans. For example, with 7 angular grid points between bore sights (both along- and across-track), a measurement block of 23 pixels across one scan can contain an angular grid of 201 by 25 pencil beams; in this example each scan is simulated using about 5000 pencil beams.
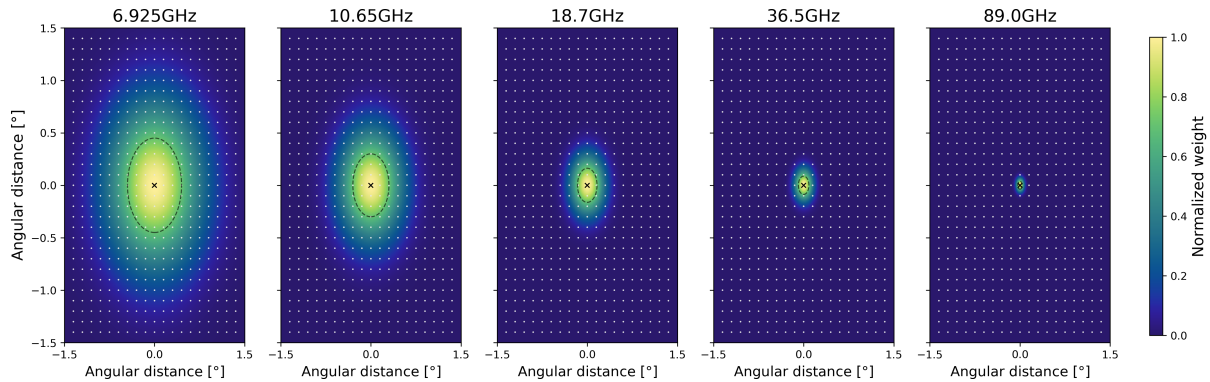
Figure 2. Antenna response in angular space for five modelled AMSR2 frequencies. The response is normalised to have a maximum value of 1.0 at the bore sight, defined by an 'x' in each panel, with angular distances defined in reference to the bore sight. The HPBW is shown by a dashed line in each panel, as defined in Table 1. The aspect ratio of the plots approximates the perspective if viewed at a $55°$ incidence angle on the Earth's surface, hence the elliptical shape. Grey dots signify a typical angular grid spacing for pencil beam calculations.

Weighting of these pencil beam calculations to synthesise the sum total T_B response of the sensor is determined by the 2D

15   antenna response, shown in Fig. 2 for five of the AMSR2 frequencies. Note that these are defined in angular space, as per the published angular beam width of each channel (Imaoka et al., 2010), assuming Gaussian response that is independent of channel polarisation. The assumption of Gaussian response with width defined by HPBW is a simplification (Maeda et al., 2016, Fig. 6). Non-negligible radiative response occurs outside the HPBW designated by ellipses in each panel, indicating that even the FOVs seen in Fig 1 can downplay the degree of overlap for AMSR2's low frequency observations. As a final step in

20   the forward model, ARTS combines the measurement blocks of each scan to create one measurement vector, containing T_Bs

for each channel at every bore sight for the desired pixels and scans. An example of the pencil beam sampling of the antenna response patterns is visible in Fig. 2 by grey dots populating the angular grid. Because of the ARTS measurement block system, each pencil beam is used for weighting various bore sights' channels and thus effectively reused, reducing overall computational cost.

5 The ocean surface emissivity model employed in the forward model is FASTEM-6, the FAST microwave Emissivity Model version 6 (Kazumori and English, 2015). FASTEM calculates sea surface emissivity and reflectivity at microwave frequencies for vertical and horizontal polarisations, taking SST, WSP, sea surface salinity, wind direction, and atmospheric transmittance as inputs. In the cases given here, salinity is prescribed as 34psu, with wind direction and transmittance either derived from ERA5 input data or prescribed in the synthetic cases. It is noted that wind direction can impact observed T_B by about $2\,\mathrm{K}$ at

10 typical wind speeds (Meissner and Wentz, 2012; Kazumori and English, 2015) and its prescription is thus a potential source of error in the observational retrieval cases.

All the retrievals described utilise 12 AMSR2 channels, foregoing the 23V and 23H channels but using all others given in Table 1. The primary sensitivity of 23V and 23H is to column water vapour because of their proximity to the $22.235\,\mathrm{GHz}$ absorption line, and water vapour is not retrieved in the inversion. Their inclusion did not adversely impact the retrieval of

15 surface parameters, but because analysis of these channels is not instructive to retrieval behaviour they were left out.

3.3 Optimal estimation module

A generic solver for inverse problems based on the optimal estimation framework (Rodgers, 2000) has been integrated into ARTS v2.3, effectively extending its functionality from a radiative transfer model to a retrieval framework. From the specification of retrieval quantities and a priori assumptions, the optimal estimation solver minimises the cost function (Eq. 1)

20 using either a Gauss-Newton or Levenberg-Marquardt optimisation method, thereby iteratively recomputing simulated observations ($f(x)$) and Jacobians ($\mathbf{K}$) as the atmospheric state is updated. Additional built-in functionality is provided to compute diagnostic quantities such as the a posteriori covariance matrix ($\mathbf{S}_x$) and averaging kernel matrix ($\mathbf{A}$).

4 Synthetic scene results

Before testing the 2DVAR methodology on real observations it was tested on a synthetic ocean scene. Synthetic observations

25 of AMSR2 channels are first simulated for the 'true' scene using the antenna patterns and sampling of Fig. 2, then random Gaussian noise is added to the synthetic measurements according to Table 1. This defines the observation vector, y. The measurement covariances ($\mathbf{S_y}$) match the noise added to y. A great advantage of the synthetic scene is that the true state ($\hat{x}$) can be constructed to match exactly the standard deviations and spatial correlations prescribed in $\mathbf{S_a}$. This ensures that the posterior errors (S_x) and averaging kernel ($\mathbf{A}$) output by the synthetic retrieval are exactly correct, whereas real retrievals

30 always contain caveats due to incomplete knowledge about the true $\mathbf{S_a}$ and $\mathbf{S_y}$. This is key to later conclusions, as $\mathbf{S_x}$ and $\mathbf{A}$ are exactly correct in the synthetic case by construction. These retrievals all use 12 channels and an observation area of 11 scans with 15 pixels from the middle of each scan.
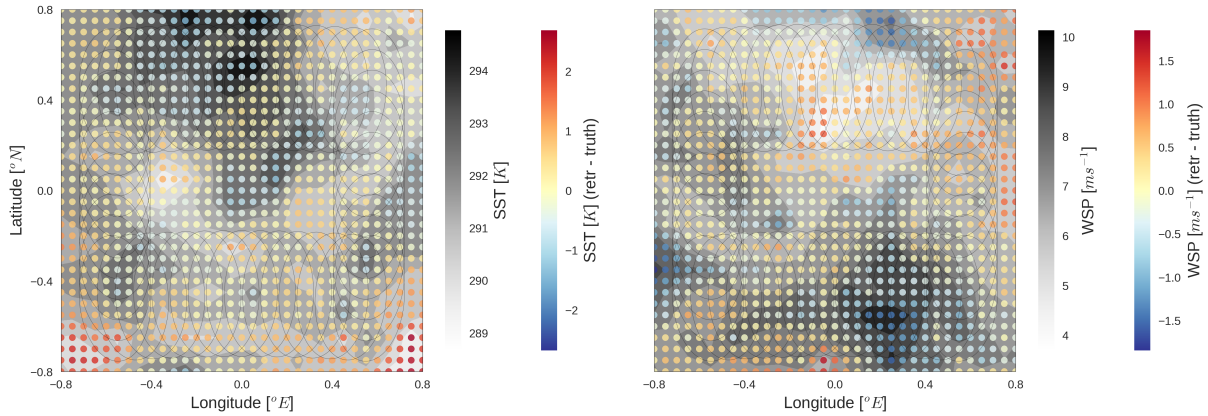
Figure 3. For the synthetic retrieval scene shown in contours, the retrieved minus true state vectors are shown for SST (left) and WSP (right). Each dot represents a retrieval grid point. FOVs for the lowest frequency channels are shown for the pixels defining the edge of the observation area.

The synthetic retrieval case described is for a priori standard deviations of 1.5 (in their respective units) and spatial decorrelation coefficients of $1.0°$, with the mean SST and WSP SI292 and $6.3\,\mathrm{m\,s^{-1}}$. Fig. 3 shows retrieved SST and WSP versus the true values, with the background contours showing the true fields, $\hat{x}$. The 6V FOVs for the outermost pixels are shown to circumscribe the observation area within the retrieval grid, which has a $0.05°$ resolution as indicated by the dots.

5   Deviations between the true and retrieved state vectors in Fig. 3 show finer spatial variability in retrieved WSP than SST despite the same prescribed covariances. This is because the random sensor noise has impacts on smaller scales for WSP, as the dominant information content for WSP comes from higher frequency channels with smaller FOVs. In contrast, the retrieved SST field is comparatively smooth relative to its true state. For both panels, deviations from $\hat{x}$ maximise outside the observation area signified by the ellipses, because there is little observational information to guide the retrieval and thus the
10 spatial correlations to the a priori state are dominant.

    From this same scene, the averaging kernels of a point near the middle of the retrieval grid are shown in Fig. 4. As with the definition of FOV, the white contour indicates where the averaging kernel drops to half of its peak value. The FOVs of the first four frequencies from Fig. 2 are overlaid in black. The bottom panels provide longitudinal and latitudinal slices through the 2D averaging kernel to demonstrate how peaked these fields are. Fig. 4 shows that the spatial resolution achieved for SST is
15 approximately circular and lies mostly within the 10GHz FOV, whereas for WSP it has a much tighter achieved resolution that is on order of the retrieval grid itself. The sum of both averaging kernels is approximately 1.0, indicating that retrieval of both variables is fully constrained by the observations.

    The companion Fig. 5 gives the difference between synthetic "observed" T_B and simulated T_B at all channels for the same retrieval case. In other words, it compares the resultant forward modelled T_B vector reached once the 2DVAR has converged
20 on a solution ($f(x)$ in Eq. 1) with the observation vector (y). Spacing of the dots in Fig. 5 demonstrates the proximity of all the observation centres. The impact of the prescribed noise on the final fit with forward modelled T_Bs is visible, manifest as a
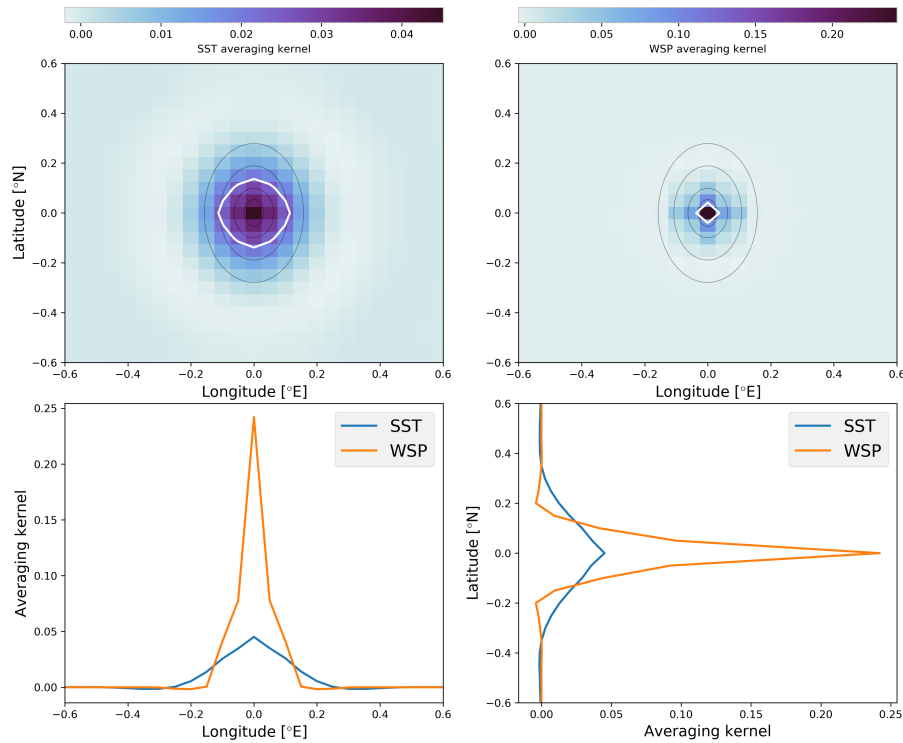
Figure 4. Averaging kernels for a central grid point from the synthetic scene, shown for SST (top left) and WSP (top right), with cross sections through the maxima given in the bottom panels. Overlaid on the top panels are the FOVs for 6, 10, 18, and 36GHz channels (in black) along with a white line indicating the half power contour of the averaging kernel.

noisy field with standard deviation approximating NEDT for each channel. In the background of the panels the SST and WSP fields are contoured as in Fig. 3, corresponding with the primary sensitivity of each channel, as the lower frequencies primarily sense SST and higher frequencies WSP. No systematic patterns are seen in the T_B differences, corresponding neither between the channels nor to the state vector differences in Fig. 3.

5   The choice of retrieval grid resolution influences the magnitude of posterior errors (Eq. 2) and some behaviour of the averaging kernels (Eq. 3) too. For the case shown, with $0.05°$ spacing, the mean posterior errors near the center of the retrieval grid are $0.59\,\text{K}$ for SST and $0.46\,\text{m s}^{-1}$ for WSP, with corresponding DFS of 24.8 and 67.1. This imbalance in DFS indicates that there is more total signal for WSP retrieval, and thus an ideal setup for these two variables would be with a finer grid spacing for WSP and a coarser grid for SST; this was not tested here, but analysis of A could guide future algorithm development and

10   selection of grid resolution for the chosen retrieval parameters. If the retrieval grid spacing is increased to $0.10°$, the posterior errors for WSP decrease slightly to $0.44\,\text{m s}^{-1}$ but its DFS also decreases to 57.0, while those for SST are almost unchanged. Thus for a coarser retrieval grid, some information on WSP is wasted despite retrieved uncertainty decreasing due to lower smoothing error, whereas it is more fitting for SST.
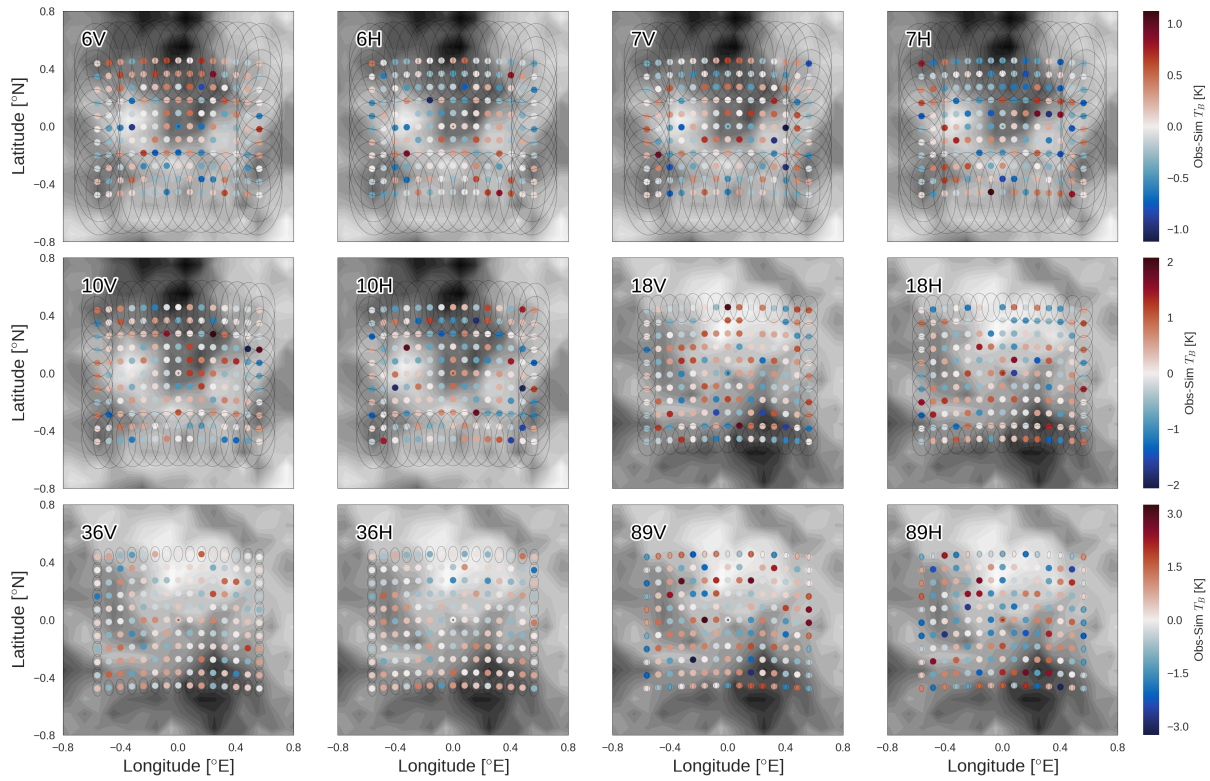
Figure 5. Observed minus simulated T_B for the 12 AMSR2 channels used in the 2DVAR for the synthetic scene. Channel names are given in each panel. Backgrounds of each panel show contours of the SST (first six panels) and WSP fields (last six panels). FOVs for each channel are shown in black as ellipses for edge pixels.

Results from this synthetic experiment with the 2DVAR retrieval indicate that convergence can be achieved in two or three iterations, with fits to T_Bs that follow the prescribed errors. Retrievals of SST and WSP are well constrained in the observation area. There is minimal influence of a priori constraints on the retrieval's behaviour within the observation area due to the high density of the observations and their overlapping information content, with elements of A summing to near 1 for all retrieval grid points within the observation area. However, for anomalies smaller than the retrieval's spatial sensitivity seen in Fig. 4, the prior still exerts some influence. This can be seen in the values of retrieved versus true SSTs in Fig. 3, where positive and negative anomalies in left centre of the SST field are not well resolved by the 2DVAR because they are slightly smaller than the achieved resolution of the retrieval. In contrast, the achieved spatial resolution for WSP is much finer due to most information coming from the higher resolution channels.

5   Observed scenes results

In this section two observed ocean scenes from September 21, 2016 are examined. These scenes were chosen because they contain significant SST and WSP gradients and featured no detectable liquid water. The first case is from an ascending orbit in the tropical Atlantic near the West African coast in the early afternoon. The second case is from a descending orbit, south of

5 Australia in the Southern Ocean in the middle of the night. The first case has high SSTs and low WSP, and is also of interest because it is near the edge of the AMSR2 scan with pixels close together, whereas the second case features high WSPs and cold SSTs. Both scenes were screened for cloud liquid water using the Remote Sensing Systems (RSS) AMSR2 v8 $0.25°$ gridded product (Hilburn and Wentz, 2008).

The focus in this section is on the match to observed T_Bs and attendant retrieval diagnostics, rather than comparison of

10 retrieved parameters with other products, as the retrieval results and sensor calibration have not been validated or tuned. Validation or comparison with values from models or other retrievals is outside the scope of this study. Instead, this section examines two distinct scenes to probe the feasibility and flexibility of the 2DVAR approach with real observational data.

The 2DVAR settings for the observed cases are quite similar to those of the synthetic retrievals described above, with the same $0.05°$ retrieval grid spacing. The a priori errors are increased to 2.0 in the respective units for both SST and WSP but

15 with the same decorrelation length of $1.0°$, so as to limit influence of the prior and not over-constrain the retrieval. Observation errors are increased to double the NEDT values along the diagonal of $\mathbf{S_y}$ to compensate somewhat for the existence of forward model and parameter errors. Also, for reasons that will become clear, $\mathbf{S_y}$ diagonal terms were adjusted for the second case presented, from twice NEDT to $50\,\mathrm{K}$ for the 6H/7H/10H channels, to effectively remove all weighting from these channels. All information on the geometry for the forward model comes from the JAXA level 1 data.

20 ### 5.1   Matching observed T_Bs

The match to observed T_Bs for the first case is shown in Fig. 6. As with the match between observed and simulated T_Bs in Fig. 5, the dots indicate observation centres and observed minus simulated T_B differences are shown for all 12 AMSR2 channels used in the 2DVAR. The observation locations come from the level 1 data, and the increased density of pixels near the edge of scan (i.e. the points located further south and west) is clearly visible.

25 Magnitudes of the T_B differences are striking in Fig. 6, with low frequency channels matching the observations within $0.5\,\mathrm{K}$ for all pixels used in the 2DVAR. The match is not much worse for the higher frequency channels either, with maximum T_B differences of $3\,\mathrm{K}$. Comparing these values with the reported sensor noise values for AMSR2 in Table 1, this is a remarkably tight fit to the observed observation vector as the fit for many channels is better than may be expected due to sensor noise alone. Given the existence of forward model errors and calibration errors as well as sensor noise, it is surprising just how well

30 the retrieval can match observed T_Bs in this scene. Despite the tight SST gradient from southwest to northeast and their large FOVs, the forward model simulates all low frequency T_Bs to a precision better than was expected even if NEDT is the only observation error source.
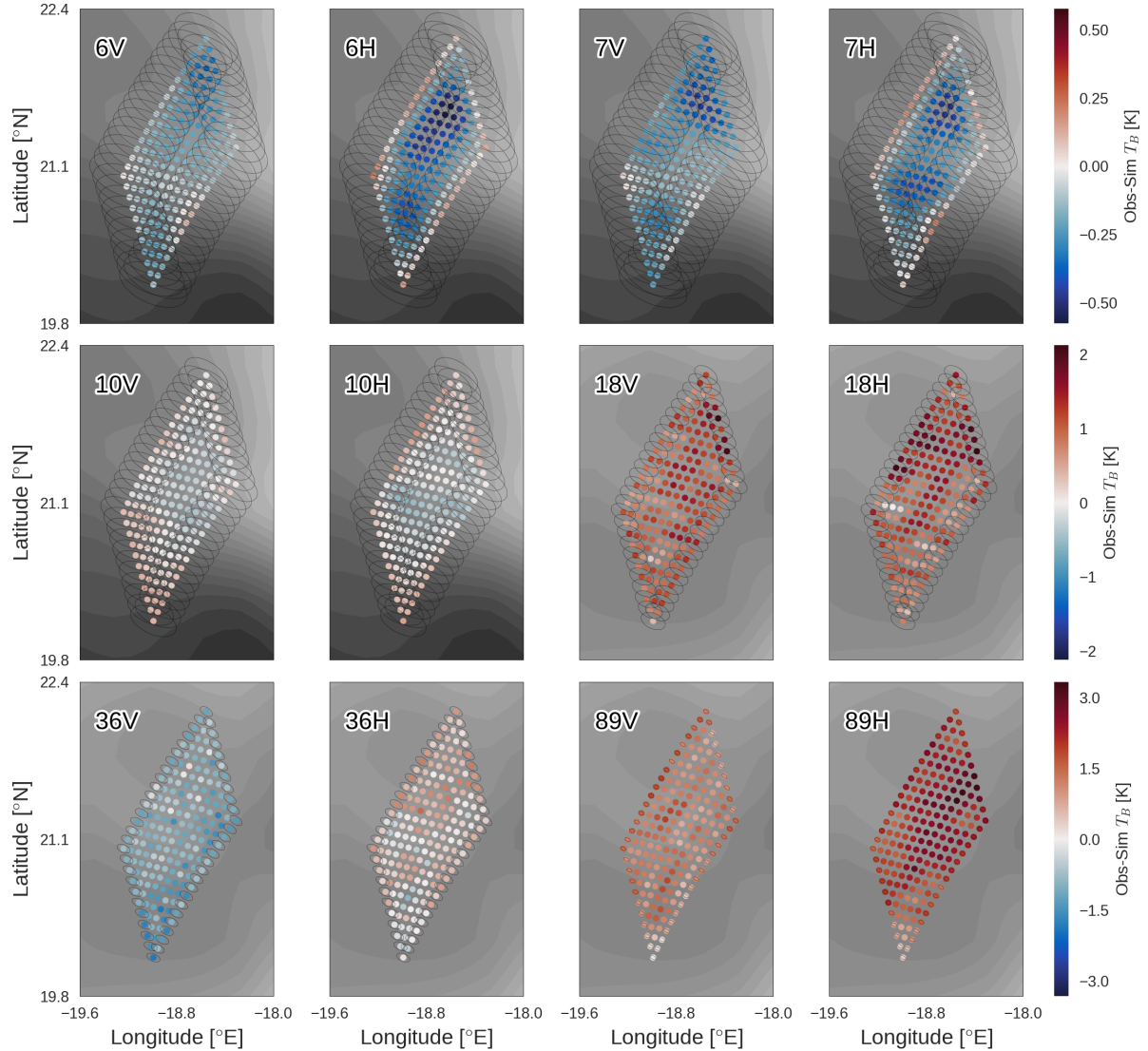
Figure 6. Observed minus simulated T_B for 12 AMSR2 channels after completion of the 2DVAR retrieval, near the coast of Mauritania in the Tropical Atlantic on September 21, 2016. The background shows SST in the first six panels and WSP in the last six, with darker colours indicating higher values. Pixels on the edge of the measurement space are plotted along with their respective FOVs.

The comparison of retrieved fields with ERA5 fields is shown in Fig. 7. Retrieved values mostly fall within the assumed errors of $2\,\mathrm{K}$ and $2\,\mathrm{m\,s^{-1}}$ with respect to ERA5 values, and demonstrate some effects at the edge of the observation space caused by the a priori spatial correlation imposed. The strong gradient in SST is largely replicated by the 2DVAR, but the retrieved results show a stronger gradient in SST in the top half of the observation space than that shown by ERA5. The

5   retrieval finds more variability in WSP than found in ERA5, with higher WSP values found on the northern and southern
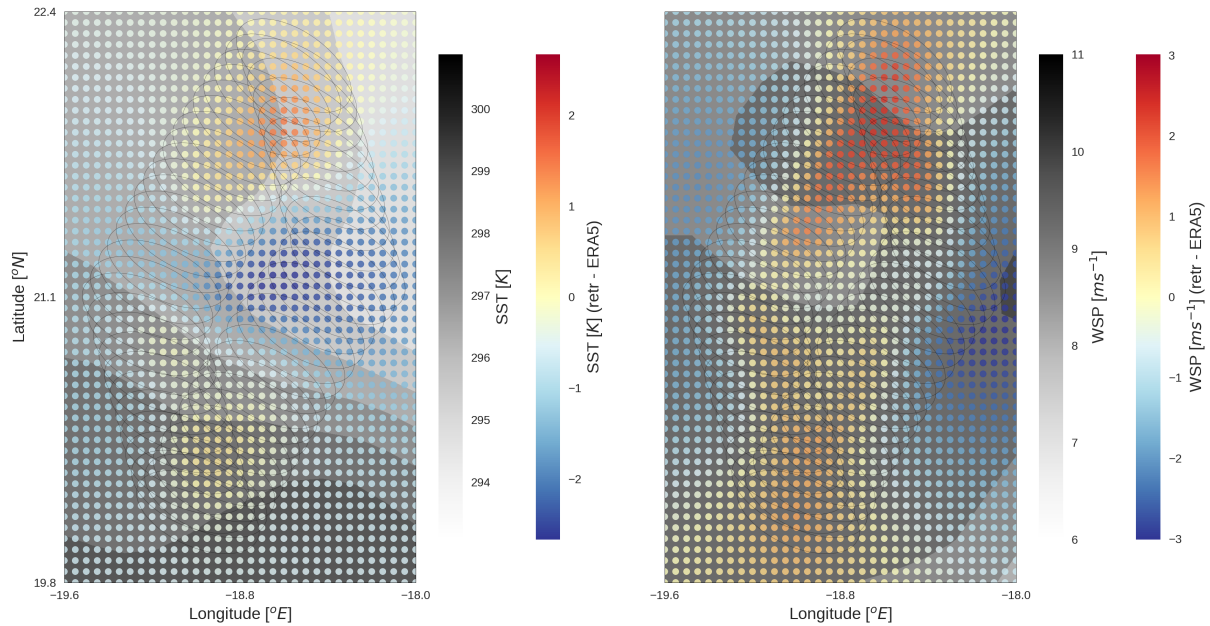
Figure 7. For the same scene as Fig. 6, the retrieved minus ERA5 state vectors are shown for SST (left) and WSP (right), with background contours showing the ERA5 fields in grayscale. Each dot represents a retrieval grid point. FOVs for the lowest frequency channels are shown for the pixels defining the edge of the observation area.

ends of the observation area. Lower SST values found in the centre of the retrieval grid appear to be driven by behaviour of the 6H/7H channels, which show small systematic negative biases in Fig. 6 that could signal a calibration issue. By the same token, the higher WSP values from the retrieval are driven partly by the positive observed minus simulated T_Bs seen at 89H.

Fig. 8 follows the same style as Fig. 6 but for the Southern Ocean case. The different magnitudes of T_B differences are
5 notable in the colour scales, as very poor fits to observed T_Bs were found at the low frequency H-pol channels of 6H, 7H, and 10H in the bottom left of the observation area. Initially the retrieval for this scene was run with the same $\mathbf{S_y}$ as the first case, but difficulties finding convergence due to the large errors at these channels caused the retrieval to be re-run with minimal weighting placed on 6H, 7H, and 10H. Through most of the observational domain, however, fits to the observations are within a few Kelvin and in line with the fits seen in Fig. 6. For instance, 89V exhibits fits within the prescribed error of double its
10 NEDT value, and most of the other V-pol channels perform similarly. The very strong diagonal gradient in WSP is manifest in the fit to T_Bs at numerous channels, hinting at emissivity model errors that are dependent on both frequency and polarisation. It seems possible that FASTEM has a low bias for the low frequency H-pol channels in the conditions of high winds and low SST, but that is speculation. The 2DVAR yields useful information in this challenging Southern Ocean case, but it highlights the importance of the emissivity model and sensor calibration.
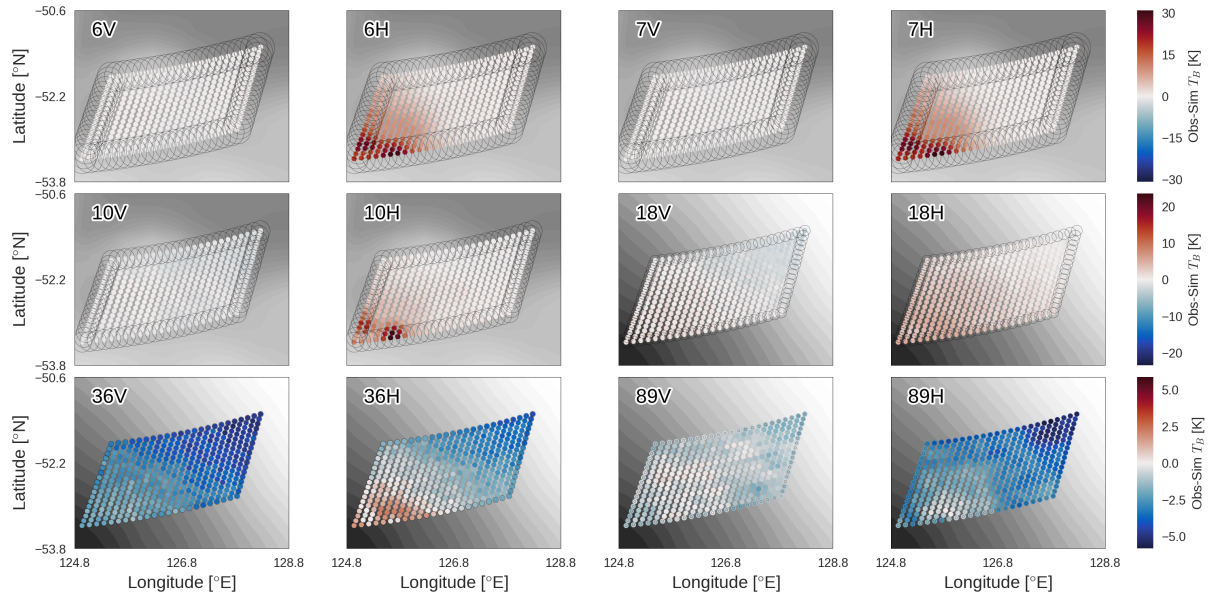
Figure 8. Observed minus simulated T_B for 12 AMSR2 channels after completion of the 2DVAR retrieval, south of Australia in the Southern Ocean on September 21, 2016. The background shows SST in the first six panels and WSP in the last six, with darker colours indicating higher values. Pixels on the edge of the measurement space are plotted along with their respective FOVs.

5.2   Retrieved spatial resolution

For the first observed case, the averaging kernels are examined to gauge the spatial resolution achieved by the 2DVAR. Shown in Fig. 9 is the averaging kernel for a retrieval grid point near the grid's centre, following the style of Fig. 4. The spatial distribution of the averaging kernels, rather elliptical and following the angular orientation of the FOVs seen describing the observational space in Fig. 6, is distinctive when compared to Fig. 4. The lower panels of Fig. 9 show less symmetry than the synthetic case examined, though the cross sections are still relatively Gaussian at this grid spacing. The overlaid contour of the averaging kernel's HPBW, with three co-located AMSR2 FOVs for references, demonstrates that the achieved spatial resolution for SST is approximately the size of the 10GHz FOVs while for WSP it is within the 18GHz FOV.

The **A** values examined in Fig. 9 are not dissimilar from those seen for the synthetic case (Fig. 4). The orientation of the sensor's spatial response is in line with the elliptical FOVs of the observations, so it is unsurprising that A follows the antenna response of the channels with the greatest sensitivity for each retrieved parameter. In terms of kilometers, the 2DVAR achieves a retrieved spatial resolution of approximately $30\,\mathrm{km}$ for SST and closer to $10\,\mathrm{km}$ for WSP. Analysis using **A** carries the caveat that not all terms are exactly known, but because these results are in line with those of the synthetic case that was constructed to yield exactly correct retrieval diagnostics, this gives confidence that Fig. 9 provides a reasonable estimate of achievable spatial resolution from a 2DVAR retrieval.
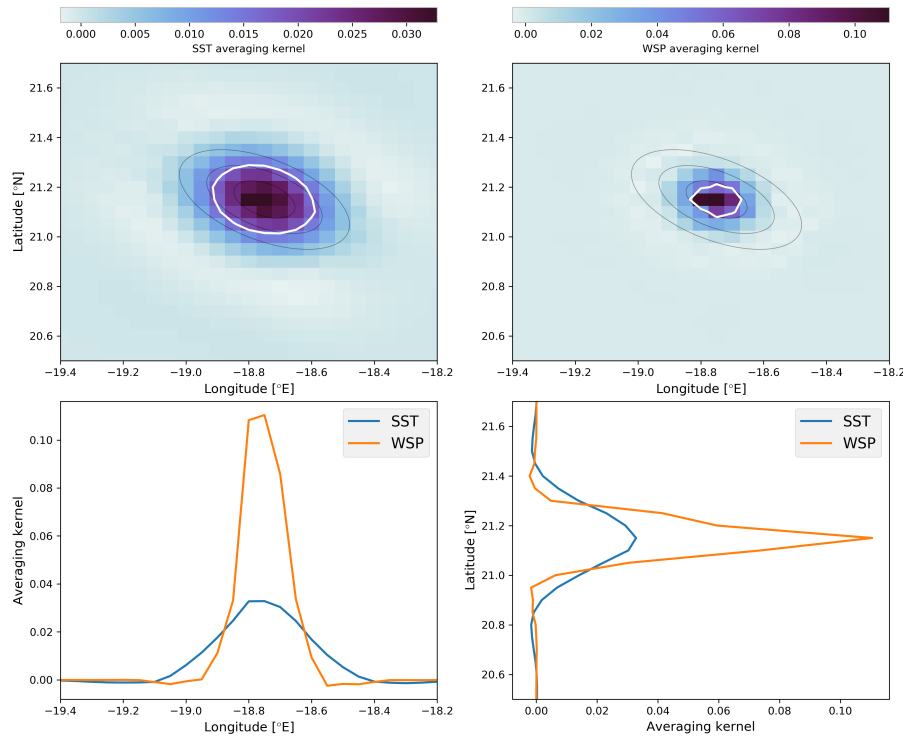
Figure 9. Averaging kernels from near the middle of the retrieval grid for the Tropical Atlantic case. The top panels show the 2D averaging kernels for SST and WSP, for one point on the retrieval grid. Overlaid are outlines of the HPBWs of 6, 10, and 18GHz channels in black, along with a contour of the half-power of the averaging kernel in white. The bottom panels show longitudinal and latitudinal transects through the centers of the plots above.

With respect to the posterior errors from the 2DVAR, those from this observed case are slightly larger than those from the synthetic case presented, as the assumed observation errors in $\mathbf{S_y}$ are larger. In the middle of the retrieval grid, mean posterior errors for SST and WSP are $0.95\,\mathrm{K}$ and $0.80\,\mathrm{m\,s^{-1}}$, respectively, for the first observed case. Posterior errors are dominated by smoothing error (Eq. 4), accounting for about two thirds of the total error for both retrieved parameters. For this case the total DFS was 77.6, of which 56.5 is for WSP and 21.1 for SST. This again demonstrates that an ideal retrieval grid spacing would thus be coarser for SST than for WSP, so as to reduce the large smoothing error seen here.

6 Discussion and conclusions

In this study a 2DVAR retrieval has been presented, inverting hundreds of T_Bs at a dozen microwave imager channels to solve for near-surface wind speed and skin temperature in oceanic scenes. To the authors' knowledge this is a novel application of the optimal estimation methodology, using explicit simulation of antenna beam patterns and spatial correlations on a fine retrieval grid to solve for an entire scene simultaneously. Whereas 2DVAR has been used in the context of scatterometer

retrievals' ambiguity removal for some time (Hoffman et al., 2003; Vogelzang and Stoffelen, 2017) the retrieval presented is a standalone 2DVAR for passive sensors. The use of 3D radiative transfer and sampling by pencil-beam calculations in the ARTS-based forward model makes the 2DVAR retrieval possible, with the full geometry of the AMSR2 sensor taken into account. While computationally expensive, the 2DVAR inversions were not prohibitively so. Retrievals of two variables on a

5     $0.05°$ grid spanning hundreds of kilometres with all channels antenna patterns simulated with high spatial fidelity took on the order of ten minutes on a desktop, with no optimisation pursued. Larger inversions would be possible with the same setup.

    A goal of this proof of concept study was to improve the spatial resolution of retrieved parameters by leveraging the spatial oversampling that is typical of low frequency microwave channels from space-borne radiometers. This goal was met, with the spatial response judged using the averaging kernel and compared against the size of different channels' FOVs in Figs. 4 and

10   9. For both the synthetic and real cases, the averaging kernels showed that the 2DVAR achieved spatial resolutions for SST on order of the 10GHz FOV, or about $30\,\mathrm{km}$. While this may not appear remarkable, it is in that most of the information content for the SST retrieval is derived from the 6 and 7GHz channels due to their greater sensitivity and lower NEDT values. For WSP the achieved spatial resolution was closer to that of the retrieval grid, smaller than the 18GHz FOV or about $10\,\mathrm{km}$. This is comparable to the real resolution achieved by current scatterometer retrievals (Vogelzang et al., 2017). Without the 2DVAR

15   approach, the spatial resolution of a microwave imager retrieval is hard to judge and may be assumed to be that of the largest FOV of all channels utilised.

    By examining the information content of the inversion via the degrees of freedom for signal, it was clear that the fine retrieval grid used in each case was suitable for WSP, but the lower DFS value for SST indicated that a coarser retrieval grid spacing would be optimal. Retrieval of both SST and WSP was well constrained by the observations, with the main influence

20   of a priori information seen in its spatial correlations and constraint outside of the observation area in Figs. 3 and 7. The overlapping information content of the low frequency channels from AMSR2 provides significant redundancy if the calibration and forward model errors are well characterised, as demonstrated by the observed versus simulated T_Bs in Figs. 6 and 8.

    The very close match to observed T_Bs exhibited in Fig. 6 was surprising for two reasons. First, it is a complex scene with a strong SST gradient in the prior, but no artifacts in the T_B fields are visible that belie this gradient. Second, the T_B fields appear

25   smoother and less variable than those of the synthetic scene (Fig. 5) despite the prescribed noise being nominally the same. This would appear to have two possible explanations, namely over-fitting from the 2DVAR or sensor noise that is not truly independent from pixel to pixel. Due to the comparison with the synthetic scene, in which T_B differences appear quite random after the 2DVAR has converged, the latter explanation seems more likely, that sensor noise is not truly random and independent across or along scans from AMSR2. If the retrieval is essentially over-estimating the sensor noise, then the posterior errors

30   reported by the 2DVAR could be over-estimates as well, and even tighter fits to observations may be possible.

    It has been argued that the methodology presented offers a more optimal use of total information content from microwave imagers than offered by T_B resampling and other retrieval methodologies. While limited in scope to cloud-free scenes in which a 2DVAR retrieval suffices, this methodology may be extended to 3DVAR standalone retrievals that encompass water vapour and hydrometeors. The 2DVAR can retrieve different parameters at the highest possible resolution permitted by the

sensor's sensitivity, with different retrieval grid resolutions, with physically consistent treatment by the forward model, and no compromises necessary in terms of target resolution or increased noise.

Utilisation of all available spectral and spatial information content from current sensors is a worthy goal for retrievals and data assimilation schemes. The results presented here demonstrate that explicit forward modeling of antenna patterns

5   can provide an alternative to the resampling methods common in the literature, with no compromises necessary such as a target resolution or increasing the noise of some channels. Instead, the 2DVAR approach permits use of all channels at their native resolution while retrieved parameters are output at the highest possible spatial resolution given the information content available. The match to observed T_Bs may also be useful in a data assimilation context, as simulation within the published noise values for the AMSR2 sensor indicates the utility of simulating the full antenna patterns with their spatial oversampling. The

10   poorer observational fit seen in Fig. 8 demonstrates that forward model errors and calibration need to be very well characterised for successful retrievals, and that an operational deployment of such a retrieval would require further development and analysis.

Code availability.   The code used for analysis is all available in the form of Jupyter notebooks via a Zenodo archive, found in the references.

Author contributions.   DD conceived of the study, performed the analysis, and wrote the manuscript. PE guided the development and SP provided technical help and discussions. The ARTS code upon which the study relies has been developed by many contributors over many

15   years, but the multivariate optimal estimation solver written by SP deserves special mention.

Competing interests.   The authors declare that they have no conflict of interest.

Acknowledgements.   This study was funded with support from the Swedish National Space Agency, for which the authors are grateful.

References

Atlas, R., Hoffman, R. N., Ardizzone, J., Leidner, S. M., Jusem, J. C., Smith, D. K., and Gombos, D.: A Cross-calibrated, Multiplatform Ocean Surface Wind Velocity Product for Meteorological and Oceanographic Applications, Bull. Amer. Meteor. Soc., 92, 157–174, https://doi.org/10.1175/2010BAMS2946.1, 2011.

5 Backus, G. E. and Gilbert, J. F.: Numerical Applications of a Formalism for Geophysical Inverse Prob., Geophys. J. R. Astron. Soc., https://doi.org/10.1111/j.1365-246X.1967.tb02159.x, 1967.

Berg, W.: GPM GMI Common Calibrated Brightness Temperatures Collocated L1C 1.5 hours 13 km V05, Tech. rep., NASA Goddard Earth Sciences Data and Information Services Center (GES DISC), Greenbelt, MD, USA, https://doi.org/10.5067/GPM/GMI/GPM/1C/05, https://disc.gsfc.nasa.gov/datasets/GPM_1CGPMGMI_05/summary, 2016.

10 Berg, W., Bilanow, S., Chen, R., Datta, S., Draper, D., Ebrahimi, H., Farrar, S., Jones, W. L., Kroodsma, R., McKague, D., Payne, V., Wang, J., Wilheit, T., and Yang, J. X.: Intercalibration of the GPM Microwave Radiometer Constellation, J. Atmos. Oceanic Technol., 33, 2639–2654, https://doi.org/10.1175/JTECH-D-16-0100.1, 2016.

Bettenhausen, M. H., Smith, C. K., Bevilacqua, R. M., Wang, N. Y., Gaiser, P. W., and Cox, S.: A nonlinear optimization algorithm for windSat wind vector retrievals, IEEE T. Geosci. Remote Sens., https://doi.org/10.1109/TGRS.2005.862504, 2006.

15 Bormann, N., Bonavita, M., Dragani, R., Eresmaa, R., Matricardi, M., and Mcnally, A.: Enhancing the impact of IASI observations through an updated observation-error covariance matrix, Quart. J. Roy. Meteor. Soc., 142, 1767–1780, https://doi.org/10.1002/qj.2774, 2016.

Boukabara, S. A., Garrett, K., Chen, W., Iturbide-Sanchez, F., Grassotti, C., Kongoli, C., Chen, R., Liu, Q., Yan, B., Weng, F., Ferraro, R., Kleespies, T. J., and Meng, H.: MiRS: An All-Weather 1DVAR Satellite Data Assimilation and Retrieval System, IEEE T. Geosci. Remote Sens., 49, 3249–3272, https://doi.org/10.1109/TGRS.2011.2158438, 2011.

20 Buehler, S. A., Mendrok, J., Eriksson, P., Perrin, A., Larsson, R., and Lemke, O.: ARTS, the Atmospheric Radiative Transfer Simulator – version 2.2, the planetary toolbox edition, Geosci. Model Dev., 11, 1537–1556, https://doi.org/10.5194/gmd-11-1537-2018, 2018.

Castro, S., Emery, W., Wick, G., and Tandy, W.: Submesoscale sea surface temperature variability from UAV and satellite measurements, Remote Sens., 9, 1089, https://doi.org/10.3390/rs9111089, 2017.

Draper, D. W.: Radio Frequency Environment for Earth-Observing Passive Microwave Imagers, IEEE J. Sel. Top. Appl. Rem. Sens., 11, 25 1–10, https://doi.org/10.1109/JSTARS.2018.2801019, 2018.

Duncan, D. I.: Supporting code for AMT submission on 2DVAR retrievals from AMSR2, https://doi.org/10.5281/zenodo.2655053, 2019.

Duncan, D. I. and Kummerow, C. D.: A 1DVAR retrieval applied to GMI: Algorithm description, validation, and sensitivities, J. Geophys. Res. Atmos., 121, 7415–7429, https://doi.org/10.1002/2016JD024808, 2016.

Duncan, D. I., Kummerow, C. D., and Meier, W. N.: An Integrated examination of AMSR2 products over ocean, IEEE J. Sel. Top. Appl. 30 Rem. Sens., 10, 3963–3974, https://doi.org/10.1109/JSTARS.2017.2718535, 2017.

Duncan, D. I., Kummerow, C. D., Dolan, B., and Petković, V.: Towards variational retrieval of warm rain from passive microwave observations, Atmos. Meas. Tech., 11, 4389–4411, https://doi.org/10.5194/amt-11-4389-2018, https://www.atmos-meas-tech.net/11/4389/2018/, 2018.

Elsaesser, G. S. and Kummerow, C. D.: Toward a fully parametric retrieval of the nonraining parameters over the global oceans, J. Appl. 35 Meteorol. and Climatol., 47, 1599–1618, https://doi.org/10.1175/2007JAMC1712.1, 2008.

Entekhabi, D., Njoku, E. G., O'Neill, P. E., Kellogg, K. H., Crow, W. T., Edelstein, W. N., Entin, J. K., Goodman, S. D., Jackson, T. J., Johnson, J., Kimball, J., Piepmeier, J. R., Koster, R. D., Martin, N., McDonald, K. C., Moghaddam, M., Moran, S., Reichle, R., Shi, J. C.,

Spencer, M. W., Thurman, S. W., Tsang, L., and Van Zyl, J.: The Soil Moisture Active Passive (SMAP) Mission, Proc. IEEE, 98, 704–716, https://doi.org/10.1109/JPROC.2010.2043918, 2010.

Eriksson, P., Buehler, S., Davis, C., Emde, C., and Lemke, O.: ARTS, the Atmospheric Radiative Transfer Simulator, version 2, J. Quant. Spectrosc. Radiat. Transfer, 112, 1551–1558, https://doi.org/10.1016/j.jqsrt.2011.03.001, 2011.

5   Geer, A., Baordo, F., Bormann, N., Chambon, P., English, S., Kazumori, M., Lawrence, H., Lean, P., Lonitz, K., and Lupu, C.: The growing impact of satellite observations sensitive to humidity, cloud and precipitation, Quart. J. Roy. Meteor. Soc., 143, 3189–3206, https://doi.org/10.1002/qj.3172, 2017.

Hilburn, K. and Wentz, F.: Intercalibrated passive microwave rain products from the unified microwave ocean retrieval algorithm (UMORA), J. Appl. Meteorol. Climatol., 47, 778–794, https://doi.org/10.1175/2007JAMC1635.1, 2008.

10 Hoffman, R. N., Leidner, S. M., Henderson, J. M., Atlas, R., Ardizzone, J. V., and Bloom, S. C.: A Two-Dimensional Variational Analysis Method for NSCAT Ambiguity Removal: Methodology, Sensitivity, and Tuning, J. Atmos. Oceanic Technol., 20, 585–605, https://doi.org/10.1175/1520-0426(2003)20<585:ATDVAM>2.0.CO;2, 2003.

Imaoka, K., Kachi, M., Fujii, H., Murakami, H., Hori, M., Ono, A., Igarashi, T., Nakagawa, K., Oki, T., Honda, Y., and Shimoda, H.: Global Change Observation Mission (GCOM) for Monitoring Carbon, Water Cycles, and Climate Change, Proc. IEEE, 98, 717–734,
15 https://doi.org/10.1109/JPROC.2009.2036869, 2010.

Kazumori, M. and English, S. J.: Use of the ocean surface wind direction signal in microwave radiance assimilation, Quart. J. Roy. Meteor. Soc., 141, 1354–1375, https://doi.org/10.1002/qj.2445, 2015.

Kazumori, M., Geer, A. J., and English, S. J.: Effects of all-sky assimilation of GCOM-W/AMSR2 radiances in the ECMWF numerical weather prediction system, Quart. J. Roy. Meteor. Soc., https://doi.org/10.1002/qj.2669, 2016.

20 Kilic, L., Prigent, C., Aires, F., Boutin, J., Heygster, G., Tonboe, R. T., Roquet, H., Jimenez, C., and Donlon, C.: Expected Performances of the Copernicus Imaging Microwave Radiometer (CIMR) for an All-Weather and High Spatial Resolution Estimation of Ocean and Sea Ice Parameters, J. Geophys. Res. Oceans, 123, 7564–7580, https://doi.org/10.1029/2018JC014408, https://agupubs.onlinelibrary.wiley.com/doi/abs/10.1029/2018JC014408, 2018.

Lin, W., Portabella, M., Stoffelen, A., Vogelzang, J., and Verhoef, A.: On mesoscale analysis and ASCAT ambiguity removal, Quart. J. Roy.
25 Meteor. Soc., 142, 1745–1756, https://doi.org/10.1002/qj.2770, https://rmets.onlinelibrary.wiley.com/doi/abs/10.1002/qj.2770, 2016.

Maeda, T., Taniguchi, Y., and Imaoka, K.: GCOM-W1 AMSR2 level 1R product: Dataset of brightness temperature modified using the antenna pattern matching technique, IEEE T. Geosci. Remote Sens., 54, 770–782, 2016.

Meier, W. N., Markus, T., Comiso, J., Ivanoff, A., and Miller, J.: AMSR2 Sea Ice Algorithm Theoretical Basis Document, Tech. rep., NASA, Cryospheric Sciences Lab, Goddard Space Flight Center, https://nsidc.org/sites/nsidc.org/files/technical-references/AMSR2_
30 SeaIce_ATBD_V2.pdf, 2017.

Meissner, T. and Wentz, F. J.: The emissivity of the ocean surface between 6 and 90 GHzover a large range of wind speeds and earth incidence angles, IEEE T. Geosci. Remote Sens., https://doi.org/10.1109/TGRS.2011.2179662, 2012.

Munchak, S. J., Meneghini, R., Grecu, M., and Olson, W. S.: A consistent treatment of microwave emissivity and radar backscatter for retrieval of precipitation over water surfaces, J. Atmos. Oceanic Technol., https://doi.org/10.1175/JTECH-D-15-0069.1, 2016.

35 Pearson, K., Merchant, C., Embury, O., and Donlon, C.: The Role of Advanced Microwave Scanning Radiometer 2 Channels within an Optimal Estimation Scheme for Sea Surface Temperature, Remote Sens., 10, https://doi.org/10.3390/rs10010090, http://www.mdpi.com/2072-4292/10/1/90, 2018.

Petty, G. W. and Bennartz, R.: Field-of-view characteristics and resolution matching for the Global Precipitation Measurement (GPM) Microwave Imager (GMI), Atmos. Meas. Tech., 10, 745–758, https://doi.org/10.5194/amt-10-745-2017, https://www.atmos-meas-tech. net/10/745/2017/, 2017.

Phalippou, L.: Variational retrieval of humidity profile, wind speed and cloud liquid-water path with the SSM/I: Potential for numerical
5   weather prediction, Quart. J. Roy. Meteor. Soc., https://doi.org/10.1256/smsqj.53001, 1996.

Rapp, A. D., Lebsock, M., and Kummerow, C.: On the consequences of resampling microwave radiometer observations for use in retrieval algorithms, J. Appl. Meteorol. Climatol., 48, 1981–1993, https://doi.org/10.1175/2009JAMC2155.1, 2009.

Reynolds, R. W., Smith, T. M., Liu, C., Chelton, D. B., Casey, K. S., and Schlax, M. G.: Daily high-resolution-blended analyses for sea surface temperature, J. Climate, https://doi.org/10.1175/2007JCLI1824.1, 2007.

10   Rodgers, C. D.: Inverse methods for atmospheric sounding: Theory and practice, vol. 2, World Scientific, 2000.

Singh, R., Pal, P. K., Kishtawal, C. M., and Joshi, P. C.: The Impact of Variational Assimilation of SSM/I and QuikSCAT Satellite Observations on the Numerical Simulation of Indian Ocean Tropical Cyclones, Weather Forecasting, 23, 460–476, https://doi.org/10.1175/2007WAF2007014.1, 2008.

The Typhon Authors: Typhon – Tools for Atmospheric Research, https://doi.org/10.5281/zenodo.1300318, https://github.com/atmtools/
15   typhon.

Vogelzang, J. and Stoffelen, A.: Two dimensional variational ambiguity removal (2DVAR), Tech. rep., KNMI, De Bilt, The Netherlands, https://www.nwpsaf.eu/publications/tech_reports/nwpsaf-kn-tr-004.pdf, 2017.

Vogelzang, J. and Stoffelen, A.: ASCAT Ultrahigh-Resolution Wind Products on Optimized Grids, IEEE J. Sel. Top. Appl. Rem. Sens., 10, 2332–2339, https://doi.org/10.1109/JSTARS.2016.2623861, 2017.

20   Vogelzang, J. and Stoffelen, A.: Improvements in Ku-band scatterometer wind ambiguity removal using ASCAT-based empirical background error correlations, Quart. J. Roy. Meteor. Soc., 144, 2245–2259, https://doi.org/10.1002/qj.3349, https://rmets.onlinelibrary.wiley.com/doi/ abs/10.1002/qj.3349, 2018.

Vogelzang, J., Stoffelen, A., Lindsley, R. D., Verhoef, A., and Verspeek, J.: The ASCAT 6.25-km Wind Product, IEEE J. Sel. Top. Appl. Rem. Sens., 10, 2321–2331, https://doi.org/10.1109/JSTARS.2016.2623862, 2017.

25   Weston, P. P., Bell, W., and Eyre, J. R.: Accounting for correlated error in the assimilation of high-resolution sounder data, Quart. J. Roy. Meteor. Soc., 140, 2420–2429, https://doi.org/10.1002/qj.2306, 2014.

Zabolotskikh, E. V., Mitnik, L. M., and Chapron, B.: Radio-Frequency Interference Identification Over Oceans for C- and X-Band AMSR2 Channels, IEEE Geosci. Remote Sens. Lett., https://doi.org/10.1109/LGRS.2015.2420120, 2015.